Quantitative Imaging of Cancer in the Postgenomic Era: Radio(geno)mics, Deep Learning, and Habitats

Sandy Napel, PhD[1], **Wei Mu, PhD**[2], **Bruna V. Jardim-Perassi, PhD**[2], **Hugo J. W. L. Aerts, PhD**[3], and **Robert J. Gillies, PhD**[2]

[1]Department of Radiology, Stanford University, Stanford, California

[2]Department of Cancer Physiology, H. Lee Moffitt Cancer Center, Tampa, Florida

[3]Dana-Farber Cancer Institute, Brigham and Women's Hospital, Harvard Medical School, Boston, Massachusetts.

Abstract

Although cancer often is referred to as "a disease of the genes," it is indisputable that the (epi)genetic properties of individual cancer cells are highly variable, even within the same tumor. Hence, preexisting resistant clones will emerge and proliferate after therapeutic selection that targets sensitive clones. Herein, the authors propose that quantitative image analytics, known as "radiomics," can be used to quantify and characterize this heterogeneity. Virtually every patient with cancer is imaged radiologically. Radiomics is predicated on the beliefs that these images reflect underlying pathophysiologies, and that they can be converted into mineable data for improved diagnosis, prognosis, prediction, and therapy monitoring. In the last decade, the radiomics of cancer has grown from a few laboratories to a worldwide enterprise. During this growth, radiomics has established a convention, wherein a large set of annotated image features (1–2000 features) are extracted from segmented regions of interest and used to build classifier models to separate individual patients into their appropriate class (eg, indolent vs aggressive disease). An extension of this conventional radiomics is the application of "deep learning," wherein convolutional neural networks can be used to detect the most informative regions and features without human intervention. A further extension of radiomics involves automatically segmenting informative subregions ("habitats") within tumors, which can be linked to underlying tumor pathophysiology. The goal of the radiomics enterprise is to provide informed decision support for the practice of precision oncology.

Keywords

Corresponding author: Robert Gillies, MD, Department of Cancer Physiology, H. Lee Moffitt Cancer Center and Research Institute, SRB-4, 12901 Magnolia Dr, Tampa, FL 33612; Robert.gillies@moffitt.org.

INTRODUCTION

Although cancer is commonly described as a "disease of the genes," it also is indisputable that the genetic and epigenetic properties of individual cancer cells are highly variable, even in different regions of the same tumor, or between metastatic sites within the same patient. By generating heterogeneous subpopulations, this genetic diversity can lead to the failure of targeted therapies or chemotherapies, even with validated targets and drugs, as resistant clones commonly emerge and proliferate. Even with the most promising of immune therapies, only approximately 10% to 20% of patients exhibit durable responses. Hence, approaches to characterize and quantify the extent of intratumoral heterogeneity in individual patients might be useful for guiding therapies that adapt during the course of treatment. Herein, we propose that a form of image-based quantitative analysis known as "radiomics" can be used to quantify heterogeneity, predict outcome, and longitudinally monitor responses.

The practice of radiology always has been focused on the interpretation of images, which, until recently, was facilitated entirely by human observation and recollection. Although there are exceptions (eg, in nuclear medicine, in which localized metabolic activity can be quantified as a specific uptake value), the characterizations of object location, shape, sharpness, and intensity are accomplished by highly trained human observers. These interpretations are critical for disease and patient management, including diagnosis, prognosis, staging, and assessment of treatment response. However, to our knowledge, with few exceptions, this is largely a subjective operation with limited specificity and high interreader variability.[1]

In 2007, Segal et al showed that careful characterization of the appearance of liver lesions in contrast-enhanced computed tomography (CT) scans could be used to reach a conclusion regarding their molecular properties.[2] Similarly, in 2008, Brown et al demonstrated that quantitative analysis of gray scale image texture on magnetic resonance imaging (MRI) scans of patients with oligodendroglioma could be used to predict their genetic signatures, specifically codeletion of chromosomes 1p and 19q.[3] These early examples indicated that not only could the appearance of noninvasive imaging be quantified, but that these data could illuminate the fundamental molecular properties of cancers. Early examples used "semantic features" (ie, categorizations of human observations using a controlled vocabulary),[4–6] and these have expanded to the use of "computational features," which are direct mathematical summarizations of image regions. Together, semantic and computational feature classes are the basis of the new field of "radiomics,"[7,8] defined as the "high-throughput extraction of quantitative features that results in the conversion of images into mineable data,"[9,10] and feature prominently in what today is called quantitative imaging.[11–13] The following section describes the radiomics workflow, including its strengths and its challenges, and highlights the integration of radiomics with clinical data and the molecular characterization of tumors, also known as radiogenomics,[14–21] for the building of predictive models. This includes both "conventional radiomics" (ie, machine computation of human-engineered image features) and artificial intelligence, or "deep learning," (DL) to automatically discover the most informative features for image phenotype description from the image and clinical data. In the second section, we discuss an emerging field, called

"habitat" imaging, which combines radiomics with multiparametric images to automatically classify the pathophysiological nature of subregions within tumors and surrounding tissues. All 3 approaches–conventional radiomics, DL, and habitat imaging–have shown high promise in predicting, making prognoses, and monitoring responses of patients with cancer to therapies.

Conventional Radiomics

Figure 1 illustrates the radiomics workflows for a volumetric data set. Component parts are: 1) the identification of the location of the subject tumor; 2) annotation of the tumor with semantic features; 3) tumor segmentation (ie, identification of the entire volume to be analyzed); and 4) image feature computation via human- engineered image features ("conventional radiomics") and/or via DL approaches ("DL radiomics"). In some cases, "delta" features[22–26] may be computed by comparing individual feature values derived from different imaging phases or images obtained at different times during the course of therapy, and/or feature vectors may be created that combine computed features from multiple imaging methods.[27–30]

Tumor identification—Each and every tumor to be processed first must be identified, either semiautomatically or manually by a radiologist or automatically using computer-aided detection approaches. When multiple tumors are present in a single imaging study, human effort generally is required to identify those that are clinically relevant, as in the case of index lesions scored with RECIST (Response Evaluation Criteria in Solid Tumors). When delta radiomics features are required, matching of tumors across observations also will be required.

Annotation with semantic features—Semantic features are descriptive observations of image content. For example, semantic features of a lung tumor might include "left lower lobe," "pleural attachment," "spiculated," "ground-glass opacity," etc. However, the extraction of semantic content from unstructured radiology reports is not appropriate due to inconsistent and/or ambiguous vocabulary across observations and observers. Furthermore, structured reports may not support the types of detailed observations required for making fine distinctions among tumor characteristics that may prove useful in classification or assessing response. Advances in structured reporting include the description of semantic features using a controlled vocabulary, such as RAD-LEX.[31] However, although much effort has been expended to develop more structured reporting, it is still not common in the broad radiology community. Currently, there are at least 2 systems that facilitate semantic annotation of radiological images using controlled vocabularies: electronic Physician Annotation Device (ePAD) (Fig. 2)[32,33] and the Annotated Image Markup (AIM) data service plug-in[34] to ClearCanvas.[35] Some semantic features, such as location, other morbidities, etc, are meant to be complementary to computational features, whereas others, such as "spherical," "heterogeneous," etc, are correlated with computational features.[36,37] One advantage of semantic annotations is that they are immediately translatable (ie, they can be ascribed in clinical environments without specialized algorithms [eg, segmentation] or workstations). As such, they have shown interesting results in several radiogenomic studies.[20,38–43]

Tumor segmentation—Radiomics features can be extracted from arbitrary regions within the image volume. A given region may contain an entire tumor, a subset of the tumor (eg, a habitat), and/or a peritumoral region thought to be involved with or affected by the tumor. In all cases, these regions must be unambiguously identified (segmented) and input to the radiomics feature computation algorithms. This segmentation step is the single most problematic aspect of conventional radiomics workflows, because the features computed from tumor volumes may be extremely sensitive to the specification of the volume to be analyzed. Each combination of tumor type and image modality presents its own challenges (including volume averaging of tissues within each voxel, tumor contrast with surrounding/adjacent structures, image contrast-to-noise characteristics, and variations of image quality across vendor implementations and time). In addition, many algorithms require operator inputs, such as bounding boxes and/or seed points, and the segmentation outlines and radiomics features computed from them may be sensitive to these inputs. For example, a recent study demonstrated wide variations in lung nodule segmentation outlines across 3 different algorithms, and even across individual algorithms initialized with different user inputs.[44] Another study using the same data set revealed that many radiomics features, particularly those that quantify shape and margin sharpness, are quite sensitive to segmentation.[45] Thus, the state of the art today is such that each segmentation must be reviewed and possibly edited by a human observer in order for the radiomics features computed from it to be trusted. One potential mitigation is to ignore segmentation altogether and to compute only features that do not require complete edge-to-edge coverage of the tumor (ie, histogram and texture features), which may be less sensitive to the exact tumor definition, and to ignore shape and margin sharpness features, which require accurate and consistent edge delineations.[46,47]

Image feature computation—Conventional or human-engineered computational image features can be divided into 4 classes, namely those that describe shape[48–50]; margin sharpness[51,52]; histogram features (eg, mean, variance, kurtosis, maximum, and minimum); and texture features,[53–60] which describe the spatial variation of gray values within the tumor. Within each class, there are hundreds to thousands of individual features: for example, some texture features quantify the spatial variation of gray values across multiple scales and orientations, and shape features can similarly quantify edge irregularity at multiple scales. It is important to recognize that many image features are intercorrelated and, as a result, not all features may add independent predictive power to radiomics models. A standard approach in many studies is to generate an autocorrelation matrix and combine correlated features into a single descriptor.[61] Several groups have made available computer code and processing pipelines for the calculation of image features from volumetric image data and segmentations (or at least volumes of interest), for example the Imaging Biomarker Explorer,[62] the Quantitative Image Feature Engine,[63] and pyRadiomics.[64]

Challenges to conventional radiomics—The ultimate usefulness of conventional radiomics workflows is to generate image features that then can be integrated with other medical data such as diagnosis, survival, response to therapy, mutations or genomic profiles, and demographics for the purposes of building predictive models for 1 of the clinical variables. Space does not allow room for details, but we note that a primary concern in these

analyses is overfitting (ie, building statistically significant models based on hundreds to thousands of image features requires data from many multiples of that number of individuals). As noted, many of the features are correlated and therefore feature reduction techniques based on redundancy, relevance, and/or sparse regression should be used wherever possible.[65,66] Although many investigators use cross-validation methods to avoid training and testing on the same data, it still is important to test each predictive model on a completely independent cohort to assess generalizability.

An additional challenge is the need to standardize the methods for the calculation of radiomics features so that identically intended features computed from the same data by different algorithms have the same name and values. Indeed, the same study referenced above that compared features computed from multiple segmentations also indicated that implementations from separate institutions of purportedly the same feature sometimes produced different values.[45] Much effort currently is underway to standardize feature naming and computation conventions, predominately led by the Image Biomarker Standardization Initiative[67] and the Quantitative Imaging Network.[11–13]

In addition to the challenges raised by segmentation, a final challenge is the sensitivity of radiomics features to image acquisition and reconstruction (ie, the heterogeneity of image acquisitions). Each clinical study uses their own combination of acquisition parameters, such as slice thickness, reconstruction kernel, MR pulse sequences, etc. In addition, many acquisition parameters are optimized for the particular patient being studied (eg, kilovoltage, mass, and field of view). Although radiologist interpretations are somewhat immune to these differences, computational radiomics features are by design sensitive to these choices. In addition, random image noise also may affect many radiomic computations.[61,68] Thus, a predictive model built for lung nodule characterization may be validated in one cohort and fail in another because of differences in the data acquisition and reconstruction. Although there have been some efforts to compensate for these differences (eg, using phantoms and image interpolation),[68–73] and herculean efforts on protocol standardization by the Quantitative Imaging Biomarkers Initiative (QIBA)[74–78] currently are underway, much work remains before radiomics analyses can derive usefulness from large databases collected by multiple institutions. Another possibility to mitigate these issues is through a branch of artificial intelligence known as DL.

Deep Learning

In conventional radiomics workflows, accurate lesion segmentation and user-defined features play key roles. As described above, there are challenges to semiautomated segmentation, such as interoperator variability and time consumption.[79–86] Although there are many hundreds of descriptive features designed by prior knowledge, the current feature sets still may not be optimal for a given task.[87]

DL can mitigate these limitations because it does not require accurate segmentation and it creates its own features through multiple layers of learning.[87–88] Only recently applied to radiomics, DL has proven to be valuable in both differential diagnosis[89–103] and prognosis.[104–107] DL involves abstraction by building networks with >2 processing layers.[108] For medical images, convolutional neural networks (CNNs) are the most common models

because they can accept 2-dimensional (2D) or 3-dimensional (3D) images as input. The first CNN was proposed by LeCun et al in 1998,[109] but its success was limited until the advent of graphic processing units and the development of learning algorithms.[93,110–112]

Figure 3 shows examples of CNNs, which can be used to classify data types as diverse as purchasing preferences and satellite images. With medical imaging, the input layer during training includes images or subregions of labeled images, which then are convolved in sublayers along with their known classifiers (for example, benign or malignant) to identify those image features that are most related to the classification. Because images contain many common features that are relevant to classification (eg, edges, shapes, colors), the core layers of CNNs relating to these can be transferred to other classification tasks. Indeed, although only recently applied in radiomics, DL has proven valuable in both differential diagnosis[89–103] and prognosis prediction.[104–107]

Two major factors influencing CNN applications in diagnostic imaging are computational power and the availability of training data. Although the solution to computing power is simply time and/or money, the solution to the limited availability of well-annotated training data sets is not so simple. One solution can be to limit the size of the input data. For example, small 2D patches can be used to significantly reduce computational costs and required training cases. Even using only 2D images, CNNs have been shown to improve accuracy compared with conventional radiomic approaches. Examples include tumor grading with MRI,[100] classification of pulmonary nodules with 2D CT,[113] and predicting response to neoadjuvant therapy with positron emission tomography (PET) images.[114]

To better use volumetric information from the 3D medical images, information from 2D patches of the 3 orthogonal views (axial, sagittal, and coronal) can be used, which is a method referred to as 2.5D.[115] These 3 views can be inputted into existing CNNs trained on 3 channels (often the red-green-blue channels of natural images).[116] If enough computational power and training cases are available, full 3D CNNs can be used to provide better results.[105,117,118] In the past 2017 Data Science Bowl focusing on lung cancer detection,[119] full 3D CNNs obtained the best performance. In addition to the different input and dimensions of the networks, many different architectures also have been attempted by incorporating unique task-specific properties such as multiview[120] and multiscale to achieve higher accuracy.[98,99,101,102,121]

An approach for solving the issue of limited data is to use "transfer learning."[122,123] This approach uses an unrelated training set to preconfigure the CNN to reduce the size of the task-specific training set. There currently are 2 popular transfer learning strategies, one of which uses an "off-the-shelf" set of CNN features and the second of which performs unsupervised pretraining on unrelated images/classification task (eg, dogs vs cats in images from the Internet) and fine-tuning on medical target images. In either strategy, a pretrained network from a larger image data set could be used as a feature extractor. The first n layers of a pretrained CNN model are used as the first n layers of a target network, and the remaining layers of the target network then are retrained toward the target task (Fig. 3). The errors from the new task can be back-propagated into the pretrained features to fine-tune them to the new task.[124] Thus, the outputs extracted from the initial layers are regarded as

meaningful features that can be used to train a separate classifier, which can include image data as well as clinical, demographic, and genomic data.[101] This has been used, for example, using the gastrointestinal stromal tumors standard graphics library[125] or bag of visual words[126] descriptors to train a CNN for chest pathology,[91,92] followed by combining generic CNN features with handcrafted features to significantly improve results in the detection of lung nodules.[127] Using a similar approach, a multiview CNN model based on a publicly available pretrained CNN-F model[128] was used for estimating a patient's risk of developing breast cancer.[94]

There also are solutions to create computerized "pseudodata" to improve the performance of DL models. This involves generating additional examples by perturbing an image by multiple transformations while keeping the class unchanged. A generic and accepted current practice is to perform geometric augmentation including image reflection, cropping, translation, and rotation. Noting that the final aim of these studies is to achieve a classification (eg, "normal" vs "cancer," "benign" vs "malignant"), when 1 class is overrepresented, only a small percentage of these cases are informative. Because the pathological classes generally are underrepresented in the cancer imaging population, using multiple transforms of these images for training the CNN can improve efficiency and accuracy.[103]

A common problem with CNNs is "overfitting," which occurs when the training set is too small compared with the number of layers or a trained model fails to generalize. This can be mitigated with regularization techniques, which add penalties for complexity or extreme parameter values.[129,130] More recently, CNN performances have been enhanced by propagating errors between layers to focus on the most robust and relevant features.[131] Several other network architectures, such as Boltzmann machine,[132] deep belief network,[133] or stacked autoencoders,[134] also have been used successfully in the detection, diagnosis, and prognosis of cancer. Although these networks can be applied to solve multiple classification problems, it is critical that the network is trained for the specific task at hand, and to test the classifier in a completely independent data set, preferably from a different institution.

Finally, and relevant to the previous and next sections, it is well known that multimodality images often provide additional information compared with those from a single modality; consequently, recent work using deep CNNs with multimodality images have attracted much attention.[132,135–137] For example, for the task of pulmonary nodule detection, Teramoto et al[136] combined CT and PET images of pulmonary nodules into a CNN and the outputs were used as inputs to 2 support vector machines, resulting in 50% fewer false-positive detections compared with a previous study.[138] In another multimodal study, a 2D CNN was trained for low-grade glioma tumor segmentation using T2, fluid-attenuated inversion recovery (FLAIR), and T1 contrast-enhanced images, and image features were obtained from its final convolutional layers. These "learned" features demonstrated improved accuracy compared with conventional radiomics for predicting *IDH1* mutation status in patients with brain cancers.[137]

Habitat Imaging

One of the most well-studied hallmarks of cancer is dysregulated angiogenesis, in which the tumor cells locally promote new blood vessels to provide nutrients and oxygen to maintain their fitness. However, because cancer cells are independently promoting local angiogenesis without regard for the rest of the tumor, a chaotic and leaky vasculature results.[139–141] This leads to stochastic and cyclical changes in blood flow[142] that, in turn, have profound effects on the local environmental properties, and the resulting evolutionary selection pressure applied to cancer cells.[143] Spatial variation in environmental stressors drives a natural selection for cells that are most fit within their specific patterns of oxygen and nutrient availability, and the buildup of acidic waste products.[143–146] Thus, these subregions, or habitats, are expected to contain cells with similar genotypes and phenotypes, including those that confer therapy resistance.[147–150] In fact, intratumoral spatial heterogeneity has been associated with resistance to therapy,[151] tumor growth,[152] and poor prognosis,[153] and therefore has direct clinical consequences. Herein, we describe approaches to characterize the presence of these habitats using multiparametric MRI (mpMRI) and emergent analyses of PET.

In this context, mpMRI can go beyond its common use to characterize tumor size and anatomy. Although response to therapy is conventionally measured by tumor size (RECIST),[154,155] functional MRI allows the assessment of tissue metabolism and physiology.[156,157] Thus, different MRI sequences can be used to measure the spatial differences in cell density, tissue organization, perfusion, and metabolism, which potentially provide earlier indications of therapeutic efficacy than tumor shrinkage as observed in size measurements.[158] The combined application of images produced by multiple MR pulse sequences (mpMRI) can simultaneously assess multiple functional processes at the cellular and molecular levels.[159] Anatomic (T2-weighted) MRI commonly is used in combination with diffusion-weighted MRI (DWI-MRI) and dynamic contrast-enhanced MRI (DCE-MRI), which are sensitive to cellularity and vascular perfusion, respectively.[160] Normally, these are evaluated independently and/or are combined into an average parameter for the entire region of interest, discarding important spatial information.[144,161] With habitat imaging, these orthogonal data sets are combined into a single parametric map. However, multiparametric analysis on a per-pixel basis to generate these maps remains challenging, because it requires spatial registration of all imaging sequences and must take into consideration resolution differences and deformations that can occur between scans.[160,162,163]

Based on the assumption that MRI scans are analogous to satellite images, the image processing technology from the National Aeronautics and Space Administration (NASA) first was adapted to segment MRI data into tissue populations as separate "scene elements." To the best of our knowledge, Vannier et al were the first to apply this methodology in a series of articles[164–166] wherein mpMRI data served as input to pattern recognition procedures implemented as feature extraction followed by classification. This enabled the production of "theme maps" through supervised and unsupervised pattern recognition procedures. By plotting the gray scale frequency distribution of each image, the data tended to form clusters, which were examined against the original MRI scans and classified with tissue characteristics. The supervised classification technique started by defining a region of

interest over the known structure, which served as a signature with which to train for the recognition of other structures that presented with the same classification. The unsupervised method analyzed mpMRI to classify tissue components without any prior information regarding the identification of the tissues. These analyses were able to differentiate brain parenchyma from hematoma, skin from cortical bone, fat from air, and cerebrospinal fluid from its surroundings. More recently, studies have evaluated intratumoral heterogeneity using specific MR images (eg, parameters derived from DWI-MRI or DCE-MRI).

DWI-MRI measures the random movements of water molecules, which are sensitive to cellular density in tissues.[159] It can be used alone or can be analyzed by calculating the apparent diffusion coefficient (ADC) using multiple diffusion weightings, which can be used as a noninvasive biomarker for diagnosis, tumor grading, and prognosis.[167,168] In addition, because changes in ADC can be observed earlier than changes in the tumor size, DWI-MRI is a useful technique for the assessment of therapy response.[159,169] Low ADC values indicate restricted diffusion, which commonly is observed in solid tumors.[170,171] Conversely, areas of necrosis and edema are expected to demonstrate high ADC values. [159,160] In preclinical studies, these data can be spatially coregistered with histology (eg, demonstrating an increase in ADC in the one-half of a prostate xenograft that received radiotherapy, which was associated with a decreased nuclear count and increase in extracellular space and nuclear size).[169] DWI-MRI scans of MDA-MB-231 and MCF-7 xenografts were used to provide quantitative texture information regarding intratumoral heterogeneity by correlating parameters derived from ADC maps with histological features. [172] In this study, histogram-based measurements of ADC values, such as standard deviation, skewness, and kurtosis, were found to be positively correlated with Ki-67 staining. Histologically defined microvessel density was found to be inversely correlated with ADC values. Thus, the less heterogeneous texture parameters derived from DWI-MRI and observed in the MDA-MB-231 xenografts corresponded to higher vascularity (CD34) and diffuse multifocal necrosis identified in histology. The incorporation of texture features derived from the combination of ADC and T2-weighted MRI increased the accuracy of the classification of Gleason patterns in patients with prostate cancer when compared with classifiers using only the ADC mean instead of the texture features.[173]

DCE-MRI reflects vascular flow and permeability by tracking the passage of a bolus injection of intravenous gadolinium-based contrast through the tissue of interest using T1-weighted images before and after the contrast administration.[174] DCE-MRI can be analyzed quantitatively by fitting the data to ad hoc or pharmacokinetic models that measure the time course of the presence of gadolinium within the tissues.[171,175] Quantitative parameters commonly reported by pharmacokinetic model–based analysis include the extracellular volume fraction (v_e) and the volume transfer constant (k^{trans}) between blood plasma and extravascular space, which is sensitive to blood flow rate and vessel permeability.[160,174] These parameters have been related to tumor angiogenesis and hypoxia by histological coregistration.[158,176–178] For example, in patients with head and neck tumors, several DCE-MRI parameters, including v_e and k^{trans}, were found to be correlated with positive staining for pimonidazole, a hypoxia tissue marker.[177] These parameters can be clustered to identify regions with different blood flow dynamics.[145,179,180] However, relevant to habitat imaging

is that the lack of perfusion would be expected to correlate to hypoxia only in areas with relatively high cell density.

The above discussion suggests that tumor habitats can be identified using different mpMRI combinations.[151,181,182] Preclinical studies are valuable because these habitats can be identified by coregistration with histology. An example is shown in Figure 4, which demonstrates that data from T2, T2* (T2star), DWI-MRI, and DCE-MRI images can be combined to identify 4 different habitats that reflect different underlying phenotypes. It is worth mentioning here that the image contrast on T2-weighted MRI is determined mainly by tissue-specific T2 relaxation times. Such images provide anatomic information and typically are used qualitatively and in mpMRI protocols. Although quantitative information also can be obtained from T2-weighted images, T2 maps provide complete quantification because signals are captured during multiple echo times and then are fit to an exponential decay curve on a pixel-by-pixel basis, yielding quantitative T2 information. The habitat map derived from mpMRI in Figure 4 shows good visual agreement with the corresponding histological slice. In this example, a 3D-printed tumor mold was used to facilitate the coregistration of the histological slices with MRI.

In other examples, k-means clustering of the ADC from DWI-MRI, T2, and M0 (proton density) images from colorectal tumor xenografts were used to follow the temporal evolution of the tumor populations in response to therapy.[181] In particular, 2 necrotic clusters were identified, both demonstrating high ADC values but differing by short or long T2 values. Necrotic regions with a long T2 value and high ADC value were confirmed as acellular, whereas the short T2 value in the other necrotic regions was ascribed to the presence of deoxyhemoglobin due to either hemorrhage or leaky vasculature. Low ADC values were found in areas of viable tumor cells and subcutaneous adipose tissue; however, viable tumor tissue exhibited lower M0 values compared with adipose. In a similar analysis, viable and necrotic areas were identified in primary tumors and metastases of a 4T1 syngeneic mouse model of breast cancer.[183] Based on the k-means clustering of ADC and T2 data, 4 clusters (2 viable and 2 necrotic areas) were identified and confirmed by histological hematoxylin and eosin staining.[182] Necrotic regions were characterized by high ADC values, but could be clustered into 2 different habitats based on their quantitative T2 values. One viable region (V1) presented with low ADC and qT2 values, whereas the other (V2) demonstrated intermediate ADC and lower qT2 values. Immunostaining of hypoxia-inducible factor 1 differentiated the 2 viable regions as well oxygenated or hypoxic subpopulations. Expression of hypoxia-inducible factor 1 was concentrated in the perinecrotic regions, classified previously as V2, which are expected to be hypoxic. The evaluation of these different viable tumor populations was informative for treatment response. Viable subregions classified as V1, which presumably are well oxygenated, demonstrated regression after irradiation, whereas the V2 subregions, characterized as hypoxic, increased, suggesting a selective survival of a subpopulation of cells resistant to radiotherapy.[151] In another study, DCE-MRI parameters were evaluated over the viable and necrotic subpopulations previously classified by the multispectral analysis of DWI-MRI, T2, and proton density. After an antiangiogenic therapy (antivascular endothelial growth factor antibody G6–31), a reduction in the K^{trans} values was observed in the viable tumor regions, whereas K^{trans} did not change in the areas classified as necrosis, and only provided noise to the DCE estimates.[184]

Clinically, mpMRI approaches are being used to identify tumor habitats, which can be used to predict outcomes for patients with cancer. In 36 patients with soft tissue sarcoma who were treated with neoadjuvant doxorubicin, the T1 postcontrast and T2 images each were divided into "high" and "low" using Otsu segmentation, and then combined to generate 4 distinct habitats: high-high, high-low, low-high, and low-low (Fig. 5).[185,186] The goal of the Otsu thresholding method is to choose the threshold that minimizes the intraclass variance. The volumes of each of these regions were entered along with multiple clinical features in a meta-analysis to predict progression-free survival (PFS) and overall survival (OS). In this, only 1 univariate predictor, the volume of the (high T1 postcontrast/low T2) habitat, was able to accurately predict OS and PFS. In cases in which this habitat occupied >18% of the tumor volume, it predicted a short PFS (P = .05) and lower OS (P = .036). In addition, these habitats could predict the existence of occult metastases with >80% accuracy. Another important aspect of these studies is that soft tissue sarcomas are a histologically heterogeneous group of diseases, but this classifier was applicable to all, regardless of histological subtype.

In patients with glioblastoma, habitat imaging can be used to segment normal from abnormal tissue. As shown in Figure 6, ADC, precontrast T1 and postcontrast T1, T2-weighted, and FLAIR images can be combined and clustered to classify tissue classes.[186,187] It has been proposed that such classifiers can be used instead of segmentation, possibly mitigating the problems discussed previously. To predict outcomes, habitat images have been generated based on postcontrast T1 and FLAIR sequences.[188] First, tumors were separated into regions of low or high contrast enhancement, based on the postcontrast T1-weighted data. Then, FLAIR values were added, thus classifying the images into 5 habitats according to different combinations of blood flow and cellularity. In this study, patients initially were divided into short-term or long-term survival groups. Long-term survivors had a predominant tumor habitat with high enhancement and intermediate cell density, whereas the tumors of short-term survivors had habitats with low enhancement and high FLAIR signals (indicating necrosis). It is interesting to note that habitats with low blood flow also exhibited cellularity comparable to that of habitats noted in regions with high blood flow, which could indicate the presence of viable cells that had adapted to survive in hypoxic and acidic conditions. More recently, these same authors presented a computational framework with which to quantitatively extract image features from the tumor habitats that demonstrated high accuracy to potentially predict the survival of patients with glioblastoma.[189] In related studies from another group, habitats in patients with glioblastoma multiforme were defined using postcontrast T1 and FLAIR data, and the spatial diversity features obtained from the habitats were associated with survival[190] as well as with the epidermal growth factor receptor expression status in patients with glioblastoma.[191]

An emerging area of interest considers the use of PET data in combination with CT or MRI to identify habitats with distinct combinations of metabolic activity (PET) with cellularity or perfusion (MRI). In patients with lung, colorectal, or breast carcinomas, subregions based on metabolic rate of glucose, which can be calculated from the pharmacokinetic analysis of dynamic PET images and is used for measuring local glucose consumption, and CT revealed a relationship between high or low metabolic regions with blood volume, cellular uptake, and washout as well as phosphorylation rate constants.[192] In a novel application of PET-

MRI, 13 patients with primary or metastatic cancers were examined with DCE-MRI and PET using [^{18}F]-galactoarginine-glycine-aspartic acid (^{18}F-galacto-RGD) (which binds to αvβ3, an integrin upregulated during angiogenesis) and [F]fludeoxyglucose (^{18}F-FDG) (glycolysis).[193] The total tumor area was divided into 4 habitats with high and low RGD and FDG uptake, respectively. Perfusion (with DCE-MRI) was noted to be highest in tumor areas with simultaneously high RGD and FDG uptake, and was restricted in areas with low uptake of both RGD and FDG. In a recent PET-MRI study of preclinical and clinical breast cancers, Gaussian mixture models combining FDG-PET and DCE-MRI were found to be able to distinguish between cystic hyperplastic, solid acinar, and solid nodular malignancies. These subregions were validated with coregistered hematoxylin and eosin staining and ex vivo autoradiography in a preclinical setting.[194]

Conclusions

In this era of personalized medicine in oncology, we have a responsibility to collect as much meaningful information from different modalities as possible, which can help to make better informed decisions. Although mutational analysis and gene expression data are indisputably important to this process, there are additional relevant data that can be used. Quantitative imaging is able to contribute significantly to decision support for 3 major reasons: 1) virtually every patient with cancer is imaged with CT, MRI, and/or PET; 2) these images are obtained from the entire tumor, along with metastases, and thus can be used to describe and classify heterogeneity; and 3) these images can be obtained routinely longitudinally to monitor responses and to guide specific therapies. As the technologies of radiomics mature, including conventional radiomics, DL, and their combination, we expect that the classifications will become more granular and will be able to identify subtumor regions ("habitats") with specific compositions of cancer cell phenotypes and genotypes, along with immune and stromal involvement, and thereby provide better options for diagnosis, staging, treatment, and monitoring of response.

Acknowledgments

CONFLICT OF INTEREST DISCLOSURES

Sandy Napel has acted as a paid member of the medical advisory boards for Fovia Inc, Radlogics Inc, and EchoPixel Inc and has acted as a paid consultant for Carestream Inc for work performed outside of the current study. In addition, Dr. Napel has a patent issued (US 9,721,340). Robert Gillies has received a grant from the National Cancer Institute for work performed as part of the current study and is an investor and board member of HealthMyne and has patents issued for Systems, Methods and Devices for Analyzing Quantitative Information Obtained from Radiological Images (PCT 9,721,340; issued August 1, 2017) and Systems and Methods for Diagnosing Tumors in a Subject By Performing a Quantitative Analysis of Texture-Based Features of a Tumor Object in a Radiological Image (PCT 9,940,709; issued April 10, 2018), and a patent pending for Radiologically Identified Tumor Habitats (15/124,718).

REFERENCES

1. Rosenkrantz AB, Ginocchio LA, Cornfeld D, et al. Interobserver reproducibility of the PI-RADS version 2 lexicon: a multicenter study of six experienced prostate radiologists. Radiology. 2016;280:793–804. [PubMed: 27035179]

2. Segal E, Sirlin CB, Ooi C, et al. Decoding global gene expression programs in liver cancer by noninvasive imaging. Nat Biotechnol. 2007;25:675–680. [PubMed: 17515910]

3. Brown R, Zlatescu M, Sijben A, et al. The use of magnetic resonance imaging to noninvasively detect genetic signatures in oligodendroglioma. Clin Cancer Res. 2008;14:2357–2362. [PubMed: 18413825]

4. Rubin DL, Mongkolwat P, Kleper V, Supekar K, Channin DS. Annotation and image markup: accessing and interoperating with the semantic content in medical imaging. IEEE Intell Syst. 2009;24:57–65.

5. Channin DS, Mongkolwat P, Kleper V, Sepukar K, Rubin DL. The caBIG annotation and image markup Project. J Digit Imaging. 2010;23:217–225. [PubMed: 19294468]

6. Rubin DL, Rodriguez C, Shah P, Beaulieu C. iPad: semantic annotation and markup of radiological images. AMIA Annu Symp Proc. 2008;626–630. [PubMed: 18999144]

7. Lambin P, Rios-Velazquez E, Leijenaar R, et al. Radiomics: extracting more information from medical images using advanced feature analysis. Eur J Cancer. 2012;48:441–446. [PubMed: 22257792]

8. Kumar V, Gu Y, Basu S, et al. Radiomics: the process and the challenges. Magn Reson Imaging. 2012;30:1234–1248. [PubMed: 22898692]

9. Gillies RJ, Kinahan PE, Hricak H. Radiomics: images are more than pictures, they are data. Radiology. 2016;278:563–577. [PubMed: 26579733]

10. Aerts HJ. The potential of radiomic-based phenotyping in precision medicine: a review. JAMA Oncol. 2016;2:1636–1642. [PubMed: 27541161]

11. Clarke LP, Nordstrom RJ, Zhang H, et al. The quantitative imaging network: NCI's historical perspective and planned goals. Transl Oncol. 2014;7:1–4. [PubMed: 24772201]

12. Nordstrom RJ. Special section guest editorial: quantitative imaging and the pioneering efforts of Laurence P. Clarke. J Med Imaging (Bellingham). 2018;5:011001. [PubMed: 28924577]

13. Nordstrom RJ. The quantitative imaging network in precision medicine. Tomography. 2016;2:239–241. [PubMed: 28083563]

14. Jamshidi N, Jonasch E, Zapala M, et al. The radiogenomic risk score stratifies outcomes in a renal cell cancer phase 2 clinical trial. Eur Radiol. 2016;26:2798–2807. [PubMed: 26560727]

15. Kuo MD, Jamshidi N. Behind the numbers: decoding molecular phenotypes with radiogenomics– guiding principles and technical considerations. Radiology. 2014;270:320–325. [PubMed: 24471381]

16. Aerts HJ, Velazquez ER, Leijenaar RT, et al. Decoding tumour phenotype by noninvasive imaging using a quantitative radiomics approach. Nat Commun. 2014;5:4006. [PubMed: 24892406]

17. Karlo CA, Di Paolo PL, Chaim J, et al. Radiogenomics of clear cell renal cell carcinoma: associations between CT imaging features and mutations. Radiology. 2014;270:464–471. [PubMed: 24029645]

18. Jamshidi N, Diehn M, Bredel M, Kuo MD. Illuminating radiogenomic characteristics of glioblastoma multiforme through integration of MR imaging, messenger RNA expression, and DNA copy number variation. Radiology. 2014;270:1–2.

19. Abazeed ME, Adams DJ, Hurov KE, et al. Integrative radiogenomic profiling of squamous cell lung cancer. Cancer Res. 2013;73:6289–6298. [PubMed: 23980093]

20. Gevaert O, Xu J, Hoang CD, et al. Non-small cell lung cancer: identifying prognostic imaging biomarkers by leveraging public gene expression microarray data–methods and preliminary results. Radiology. 2012;264:387–396. [PubMed: 22723499]

21. Rutman AM, Kuo MD. Radiogenomics: creating a link between molecular diagnostics and diagnostic imaging. Eur J Radiol. 2009;70:232–241. [PubMed: 19303233]

22. van Timmeren JE, Leijenaar RTH, van Elmpt W, Reymen B, Lambin P. Feature selection methodology for longitudinal conebeam CT radiomics. Acta Oncol. 2017;56:1537–1543. [PubMed: 28826307]

23. Bakr S, Echegaray S, Shah R, et al. Noninvasive radiomics signature based on quantitative analysis of computed tomography images as a surrogate for microvascular invasion in hepatocellular carcinoma: a pilot study. J Med Imaging (Bellingham). 2017;4:041303. [PubMed: 28840174]

24. Huang Q, Lu L, Dercle L, et al. Interobserver variability in tumor contouring affects the use of radiomics to predict mutational status. J Med Imaging (Bellingham). 2018;5:011005. [PubMed: 29098170]

25. Fave X, Zhang L, Yang J, et al. Using pretreatment radiomics and delta-radiomics features to predict non-small cell lung cancer patient outcomes [abstract]. Int J Radiat Oncol Biol Phys. 2017;98:249.

26. Fave X, Zhang L, Yang J, et al. Delta-radiomics features for the prediction of patient outcomes in non-small cell lung cancer. Sci Rep. 2017;7:588. [PubMed: 28373718]

27. Gevaert O, Mitchell LA, Achrol AS, et al. Glioblastoma multiforme: exploratory radiogenomic analysis by using quantitative image features. Radiology. 2015;276:313. [PubMed: 26101929]

28. Itakura H, Achrol AS, Mitchell LA. Magnetic resonance image features identify glioblastoma phenotypic subtypes with distinct molecular pathway activities. Sci Transl Med. 2015;7:303ra138.

29. Zinn PO, Mahajan B, Sathyan P, et al. Radiogenomic mapping of edema/cellular invasion MRI-phenotypes in glioblastoma multiforme. PLoS One. 2011;6:e25451. [PubMed: 21998659]

30. Li Q, Bai H, Chen Y, et al. A fully-automatic multiparametric radiomics model: towards reproducible and prognostic imaging signature for prediction of overall survival in glioblastoma multiforme. Sci Rep. 2017;7:14331. [PubMed: 29085044]

31. Langlotz CP. RadLex: a new method for indexing online educational materials. Radiographics. 2006;26:1595–1597. [PubMed: 17102038]

32. Rubin DL, Willrett D, O'Connor MJ, Hage C, Kurtz C, Moreira DA. Automated tracking of quantitative assessments of tumor burden in clinical trials. Transl Oncol. 2014;7:23–35. [PubMed: 24772204]

33. National Cancer Institute. AIM Template Builder 2.0 user's guide. https://wiki.nci.nih.gov/display/AIM/AIM+Template+Builder+2.0+User%27s+Guide. Accessed April 12, 2018.

34. Ronden MI, van Sornsen de Koste JR, Johnson C, et al. Incidence of high-risk radiologic features in patients without local recurrence after stereotactic ablative radiation therapy for early-stage non-small cell lung cancer. Int J Radiat Oncol Biol Phys. 2018;100:115–121. [PubMed: 29102278]

35. Roy S, Brown MS, Shih GL. Visual Interpretation with Three-Dimensional Annotations (VITA): 3-dimensional image interpretation tool for radiological reporting. J Digit Imaging. 2014;27:49–57. [PubMed: 23979113]

36. Depeursinge A, Kurtz C, Beaulieu C, Napel S, Rubin D. Predicting visual semantic descriptive terms from radiological image data: preliminary results with liver lesions in CT. IEEE Trans Med Imaging. 2014;33:1669–1676. [PubMed: 24808406]

37. Yip SSF, Liu Y, Parmar C, et al. Associations between radiologist-defined semantic and automatically computed radiomic features in non-small cell lung cancer. Sci Rep. 2017;7:3519. [PubMed: 28615677]

38. Gevaert O, Echegaray S, Khuong A, et al. Predictive radiogenomics modeling of EGFR mutation status in lung cancer. Sci Rep. 2017;7:41674. [PubMed: 28139704]

39. Banerjee S, Wang DS, Kim HJ, et al. A computed tomography radiogenomic biomarker predicts microvascular invasion and clinical outcomes in hepatocellular carcinoma. Hepatology. 2015;62:792–800. [PubMed: 25930992]

40. Jamshidi N, Jonasch E, Zapala M, et al. The radiogenomic risk score: construction of a prognostic quantitative, noninvasive image-based molecular assay for renal cell carcinoma. Radiology. 2015;277:114–123. [PubMed: 26402495]

41. Liu Y, Balagurunathan Y, Atwater T, et al. Radiological image traits predictive of cancer status in pulmonary nodules. Clin Cancer Res. 2017;23:1442–1449. [PubMed: 27663588]

42. Liu Y, Kim J, Qu F, et al. CT features associated with epidermal growth factor receptor mutation status in patients with lung adenocarcinoma. Radiology. 2016;280:271–280. [PubMed: 26937803]

43. Grossmann P, Stringfield O, El-Hachem N. Defining the biological basis of radiomic phenotypes in lung cancer. Elife. 2017;60.

44. Kalpathy-Cramer J, Zhao B, Goldgof D, et al. A comparison of lung nodule segmentation algorithms: methods and results from a multi-institutional study. J Digit Imaging. 2016;29:476–487. [PubMed: 26847203]

45. Kalpathy-Cramer J, Mamomov A, Zhao B, et al. Radiomics of lung nodules: a multi-institutional study of robustness and agreement of quantitative imaging features. Tomography. 2016;2:430–437. [PubMed: 28149958]

46. Echegaray S, Gevaert O, Shah R, et al. Core samples for radiomics features that are insensitive to tumor segmentation: method and pilot study using CT images of hepatocellular carcinoma. J Med Imaging (Bellingham). 2015;2:041011. [PubMed: 26587549]

47. Echegaray S, Nair V, Kadoch M, et al. A rapid segmentation-insensitive "digital biopsy" method for radiomic feature extraction: method and pilot study using CT images of non-small cell lung cancer. Tomography. 2016;2:283–294. [PubMed: 28612050]

48. Xu J, Faruque J, Beaulieu CF, Rubin D, Napel S. A comprehensive descriptor of shape: method and application to content-based retrieval of similar appearing lesions in medical images. J Digit Imaging. 2012;25:121–128. [PubMed: 21547518]

49. Bankman IN, Spisz TS, Pavlapoilos S. Two-dimensional shape and texture quantification In: Bankman, ed. Handbook of Medical Image Processing and Analysis. Amsterdam: Elsevier/Academic Press 2009:261–277.

50. Grove O, Berglund AE, Schabath MB, et al. Quantitative computed tomographic descriptors associate tumor shape complexity and intratumor heterogeneity with prognosis in lung adenocarcinoma. PLoS One. 2015;10:e0118261. [PubMed: 25739030]

51. Xu J, Napel S, Greenspan H, Beaulieu CF, Agrawal N, Rubin D. Quantifying the margin sharpness of lesions on radiological images for content-based image retrieval. Med Phys. 2012;39:5405–5418. [PubMed: 22957608]

52. Mu T, Nandi AK, Rangayyan RM. Classification of breast masses using selected shape, edge-sharpness, and texture features with linear and kernel-based classifiers. J Digit Imaging. 2008;21:153–169. [PubMed: 18306000]

53. Zayed N, Elnemr HA. Statistical analysis of haralick texture features to discriminate lung abnormalities. Int J Biomed Imaging. 2015;2015:267807. [PubMed: 26557845]

54. Yang D, Rao G, Martinez J, Veeraraghavan A, Rao A. Evaluation of tumor-derived MRI-texture features for discrimination of molecular subtypes and prediction of 12-month survival status in glioblastoma. Med Phys. 2015;42:6725–6735. [PubMed: 26520762]

55. Vallieres M, Freeman CR, Skamene SR, El Naqa I. A radiomics model from joint FDG-PET and MRI texture features for the prediction of lung metastases in soft-tissue sarcomas of the extremities. Phys Med Biol. 2015;60:5471–5496. [PubMed: 26119045]

56. Liu H, Tan T, van Zelst J, Mann R, Karssemeijer N, Platel B. Incorporating texture features in a computer-aided breast lesion diagnosis system for automated three-dimensional breast ultrasound. J Med Imaging (Bellingham). 2014;1:024501. [PubMed: 26158036]

57. Korfiatis P, Kline TL, Coufalova L, et al. MRI texture features as biomarkers to predict MGMT methylation status in glioblastomas. Med Phys. 2016;43:2835–2844. [PubMed: 27277032]

58. Depeursinge A, Yanagawa M, Leung AN, Rubin DL. Predicting adenocarcinoma recurrence using computational texture models of nodule components in lung CT. Med Phys. 2015;42:2054–2063. [PubMed: 25832095]

59. Depeursinge A, Foncubierta-Rodriguez A, Van de Ville D, Muller H. Rotation-covariant texture learning using steerable riesz wavelets. IEEE Trans Image Process. 2014;23:898–908. [PubMed: 26270926]

60. Wibmer A, Hricak H, Gondo T, et al. Haralick texture analysis of prostate MRI: utility for differentiating non-cancerous prostate from prostate cancer and differentiating prostate cancers with different Gleason scores. Eur Radiol. 2015;25:2840–2850. [PubMed: 25991476]

61. Balagurunathan Y, Kumar V, Gu Y, et al. Test-retest repro-ducibility analysis of lung CT image features. J Digit Imaging. 2014;27:805–823. [PubMed: 24990346]

62. Zhang L, Fried DV, Fave XJ, Hunter LA, Yang J, Court LE. IBEX: an open infrastructure software platform to facilitate collaborative work in radiomics. Med Phys. 2015;42:1341–1353. [PubMed: 25735289]

63. Echegaray S, Bakr S, Rubin DL, Napel S. Quantitative Image Feature Engine (QIFE): an open-source, modular engine for 3d quantitative feature extraction from volumetric medical images [published online ahead of print October 6, 2017]. J Digit Imaging. 2017. doi: 10.1007/s10278-017-0019-x.

64. van Griethuysen JJ, Fedorov A, Parmar C, et al. Computational radiomics system to decode the radiographic phenotype. Cancer Res. 2017;77:e104–e107. [PubMed: 29092951]

65. Peng HC, Long FH, Ding C. Feature selection based on mutual information: criteria of max-dependency, max-relevance, and min-redundancy. IEEE Trans Pattern Anal Mach Intell. 2005;27:1226–1238. [PubMed: 16119262]

66. Tibshirani R Regression shrinkage and selection via the Lasso. J R Stat Soc B. 1996;58:267–288.

67. Zwanenburg A, Leger S, Vallieres M, Lock S. Image biomarker standardisation initiative. arXiv preprint arXiv:1612.07003v6. 2018.

68. Solomon J, Mileto A, Nelson RC, Roy Choudhury K, Samei E. Quantitative features of liver lesions, lung nodules, and renal stones at multi-detector row CT examinations: dependency on radiation dose and reconstruction algorithm. Radiology. 2016;279:185–194. [PubMed: 26624973]

69. Fave X, Mackin D, Yang J, et al. Can radiomics features be reproducibly measured from CBCT images for patients with non-small cell lung cancer? Med Phys. 2015;42:6784–6797. [PubMed: 26632036]

70. Yasaka K, Akai H, Mackin D, et al. Precision of quantitative computed tomography texture analysis using image filtering: a phantom study for scanner variability. Medicine (Baltimore). 2017;96:e6993. [PubMed: 28538408]

71. Shafiq-Ul-Hassan M, Zhang GG, Latifi K, et al. Intrinsic dependencies of CT radiomic features on voxel size and number of gray levels. Med Phys. 2017;44:1050–1062. [PubMed: 28112418]

72. Mackin D, Fave X, Zhang L, et al. Harmonizing the pixel size in retrospective computed tomography radiomics studies. PLoS One. 2017;12:e0178524. [PubMed: 28934225]

73. Mackin D, Fave X, Zhang L, et al. Measuring computed tomography scanner variability of radiomics features. Invest Radiol. 2015;50:757–765. [PubMed: 26115366]

74. Sullivan DC, Obuchowski NA, Kessler LG, et al. Metrology standards for quantitative imaging biomarkers. Radiology. 2015;277:813–825. [PubMed: 26267831]

75. Obuchowski NA, Buckler A, Kinahan P, et al. Statistical issues in testing conformance with the Quantitative Imaging Biomarker Alliance (QIBA) profile claims. Acad Radiol. 2016;23:496–506. [PubMed: 26898527]

76. Kessler LG, Barnhart HX, Buckler AJ, et al. QIBA Terminology Working Group. The emerging science of quantitative imaging biomarkers terminology and definitions for scientific studies and regulatory submissions. Stat Methods Med Res. 2015;24:9–26. [PubMed: 24919826]

77. Chen-Mayer HH, Fuld MK, Hoppel B, et al. Standardizing CT lung density measure across scanner manufacturers. Med Phys. 2017;44:974–985. [PubMed: 28060414]

78. Chao SL, Metens T, Lemort M. TumourMetrics: a comprehensive clinical solution for the standardization of DCE-MRI analysis in research and routine use. Quant Imaging Med Surg. 2017;7:496–510. [PubMed: 29184762]

79. Foster B, Bagci U, Mansoor A, Xu Z, Mollura DJ. A review on segmentation of positron emission tomography images. Comput Biol Med. 2014;50:76–96. [PubMed: 24845019]

80. Clarke L, Velthuizen R, Camacho M, et al. MRI segmentation: methods and applications. Magn Reson Imaging. 1995;13:343–368. [PubMed: 7791545]

81. Mansoor A, Bagci U, Foster B, et al. Segmentation and image analysis of abnormal lungs at CT: current approaches, challenges, and future trends. Radiographics. 2015;35:1056–1076. [PubMed: 26172351]

82. Pham DL, Xu C, Prince JL. Current methods in medical image segmentation. Annu Rev Biomed Eng. 2000;2:315–337. [PubMed: 11701515]

83. Withey DJ, Koles ZJ. A review of medical image segmen-tation: methods and available software. Int J Bioelectromagn. 2008;10:125–148.

84. Punia R, Singh S. Review on machine learning techniques for automatic segmentation of liver images. Int J Adv Res Comput Sci Softw Eng. 2013;3:666–670.

85. Petitjean C, Dacher JN. A review of segmentation methods in short axis cardiac MR images. Med Image Anal. 2011;15:169–184. [PubMed: 21216179]

86. Cabezas M, Oliver A, Llado X, Freixenet J, Cuadra MB. A review of atlas-based segmentation for magnetic resonance brain images. Comput Methods Programs Biomed. 2011;104:e158–e177. [PubMed: 21871688]

87. Shen D, Wu G, Suk HI. Deep learning in medical image analysis. Annu Rev Biomed Eng. 2017;21:221–248.

88. Suzuki K Overview of deep learning in medical imaging. Radiol Phys Technol. 2017;10:257–273. [PubMed: 28689314]

89. Anthimopoulos M, Christodoulidis S, Ebner L, Christe A, Mougiakakou S. Lung pattern classification for interstitial lung diseases using a deep convolutional neural network. IEEE Trans Med Imaging. 2016;35:1207–1216. [PubMed: 26955021]

90. Armato SG, McLennan G, Bidaut L, et al. The Lung Image Database Consortium (LIDC) and Image Database Resource Initiative (IDRI): a completed reference database of lung nodules on CT scans. Med Phys. 2011;38:915–931. [PubMed: 21452728]

91. Bar Y, Diamant I, Wolf L, GreenspanH. Deep learning with non-medical training used for chest pathology identification. Proc SPIE. 2015;94140V.

92. Bar Y, Diamant I, Wolf L, Lieberman S, Konen E, Greenspan H. Chest pathology detection using deep learning with non-medical training. Proc Int Symp Biomed Imaging. 2015;294–297.

93. Bengio Y, Lamblin P, Popovici D, Larochelle H. Greedy lay-er-wise training of deep networks. Proc Neural Inf Process Syst. 2006;153–160.

94. Carneiro G, Nascimento J, Bradley AP. Unregistered multiview mammogram analysis with pre-trained deep learning models. Med Image Comput Comput Assist Interv. 2015;652–660.

95. Hosseini-Asl E, Gimel'farb G, El-Baz A.Alzheimer's disease diagnostics by a deeply supervised adaptable 3D convolutional network. arXiv preprint arXiv:1607.00556. 2016.

96. Jiang H, Ma H, Qian W, Gao M, Li Y An automatic detection system of lung nodule based on multi-group patch-based deep learning network [published online ahead of print July 14, 2017]. IEEE J Biomed Health Inform. doi: 10.1109/JBHI.2017.2725903.

97. Kawahara J, BenTaieb A, Hamarneh G. Deep features to classify skin lesions. Proc Int Symp Biomed Imaging. 2016;1397–1400.

98. Zhen X, Wang Z, Islam A, Bhaduri M, Chan I, Li S. Multi-scale deep networks and regression forests for direct bi-ventricular volume estimation. Med Image Anal. 2016;30:120–129. [PubMed: 26919699]

99. Lotter W, Sorensen G, Cox D. A multi-scale CNN and curriculum learning strategy for mammogram classification. Proc Deep Learn Med Image Anal. 2017:169–177.

100. Pan Y, Huang W, Lin Z, et al. Brain tumor grading based on neural networks and convolutional neural networks. Proc Eng Med Biol Conf. 2015; 699–702.

101. Schlegl T, Waldstein SM, Vogl WD, Schmidt-Erfurth U, Langs G. Predicting semantic descriptions from medical images with convolutional neural networks. Inf Process Med Imaging. 2015;24:437–448. [PubMed: 26221693]

102. Shen W, Zhou M, Yang F, Yang C, Tian J. Multi-scale convolutional neural networks for lung nodule classification. Inf Process Med Imaging. 2015;24:588–599. [PubMed: 26221705]

103. van Grinsven MJ, van Ginneken B, Hoyng CB, Theelen T, Sanchez CI. Fast convolutional neural network training using selective data sampling: application to hemorrhage detection in color fundus images. IEEE Trans Med Imaging. 2016;35:1273–1284. [PubMed: 26886969]

104. Kawahara J, Brown CJ, Miller SP, et al. BrainNetCNN: convolutional neural networks for brain networks; towards predicting neurodevelopment. Neuroimage. 2017;146:1038–1049. [PubMed: 27693612]

105. Nie D, Zhang H, Adeli E, Liu L, Shen D. 3D deep learning for multi-modal imaging-guided survival time prediction of brain tumor patients. Medical Image Comput Comput Assist Interv. 2016;9901:212–220.

106. Yoo Y, Tang LW, Brosch T, et al. Deep learning of brain lesion patterns for predicting future disease activity in patients with early symptoms of multiple sclerosis. Proc Deep Learn Med Image Anal. 2016;86–94.

107. van der Burgh HK, Schmidt R, Westeneng HJ, de Reus MA, van den Berg LH, van den Heuvel MP. Deep learning predictions of survival based on MRI in amyotrophic lateral sclerosis. Neuroimage Clin. 2017;13:361–369. [PubMed: 28070484]

108. LeCun Y, Bengio Y, Hinton G. Deep learning. Nature. 2015;521:436–444. [PubMed: 26017442]

109. LeCun Y, Bottou L, Bengio Y, Haffner P. Gradient-based learning applied to document recognition. Proc. IEEE. 1998;86: 2278–2324.

110. Poultney C, Chopra S, Cun YL. Efficient learning of sparse representations with an energy-based model. Proc Neural Inf Process Syst. 2007;1137–1144.

111. Hinton GE, Salakhutdinov RR. Reducing the dimensionality of data with neural networks. Science. 2006;313:504–507. [PubMed: 16873662]

112. Trebeschi S, van Griethuysen JJM, Lambregts DMJ, et al. Deep learning for fully-automated localization and segmentation of rectal cancer on multiparametric MR. Sci Rep. 2017;7:5301. [PubMed: 28706185]

113. Li W, Cao P, Zhao D, Wang J. Pulmonary nodule classification with deep convolutional neural networks on computed tomography images. Comput Math Methods Med. 2016;2016:6215085. [PubMed: 28070212]

114. Ypsilantis PP, Siddique M, Sohn HM, et al. Predicting response to neoadjuvant chemotherapy with PET imaging using convolutional neural networks. PLoS One. 2015;10:e0137036. [PubMed: 26355298]

115. Roth HR, Lu L, Liu J, et al. Improving computer-aided detection using convolutional neural networks and random view aggregation. IEEE Trans Med Imaging. 2016;35:1170–1181. [PubMed: 26441412]

116. Buty M, Xu Z, Gao M, Bagci U, Wu A, Mollura DJ. Characterization of lung nodule malignancy using hybrid shape and appearance features. Proc Med Image Comput Comput Assist Interv. 2016;662–670.

117. Chen H, Yu L, Dou Q, Shi L, Mok VC, Heng PA. Automatic detection of cerebral microbleeds via deep learning based 3d feature representation. Proc Int Symp Biomed Imaging. 2015;764–767.

118. Kamnitsas K, Ledig C, Newcombe VFJ, et al. Efficient multi-scale 3D CNN with fully connected CRF for accurate brain lesion segmentation. Med Image Anal. 2017;36:61–78. [PubMed: 27865153]

119. Kaggle. Kaggle Data Science Bowl 2017. 2017 https://www.kaggle.com/c/data-science-bowl-2017. Accessed April 26, 2017.

120. Setio AA, Ciompi F, Litjens G, et al. Pulmonary nodule detection in CT images: false positive reduction using multi-view convolutional networks. IEEE Trans Med Imaging. 2016;35:1160–1169. [PubMed: 26955024]

121. Shin HC, Roth HR, Gao M, et al. Deep convolutional neural networks for computer-aided detection: CNN architectures, dataset characteristics and transfer learning. IEEE Trans Med Imaging. 2016;35:1285–1298. [PubMed: 26886976]

122. van Opbroek A, Ikram MA, Vernooij MW, de Bruijne M. Transfer learning improves supervised image segmentation across imaging protocols. IEEE Trans Med Imaging. 2015;34:1018–1030. [PubMed: 25376036]

123. Razavian AS, Azizpour H, Sullivan J, Carlsson S. CNN features off-the-shelf: an astounding baseline for recognition. arXiv preprint arXiv:1403.6382v3. 2014.

124. Yosinski J, Clune J, Bengio Y, Lipson H. How transferable are features in deep neural networks? Adv. Neural Inf Process Syst 2014;3320–3328.

125. Oliva A, Torralba A. Modeling the shape of the scene: a holistic representation of the spatial envelope. Int J Comput Vision. 2001;42:145–175.

126. Csurka G, Dance C, Fan L, Willamowski J, Bray C. Visual categorization with bags of keypoints. Workshop on statistical learning in computer vision, ECCV: Prague, 2004:1–2.

127. van Ginneken B, Setio AA, Jacobs C, Ciompi F. Off-the-shelf convolutional neural network features for pulmonary nodule detection in computed tomography scans. Proc Int Symp Biomed Imaging. 2015:286–289.

128. Chatfield K, Simonyan K, Vedaldi A, Zisserman A. Return of the devil in the details: delving deep into convolutional nets. arXiv preprint arXiv:1405.3531. 2014.

129. Srivastava N, Hinton GE, Krizhevsky A, Sutskever I, Salakhutdinov R. Dropout: a simple way to prevent neural networks from overfitting. J Mach Learning Res. 2014;15:1929–1958.

130. Krizhevsky A, Sutskever I, Hinton GE. Imagenet classification with deep convolutional neural networks. Proc Neural Inf Process Syst. 2012;1097–1105.

131. Ozdenirm O, Woodward B, Berlin AA. Propagating Uncertainty in Multi-Stage Bayesian Convolutional Neural Networks with Application to Pulmonary Nodule Detection. Proc Neural Inf Process Syst Conf Bayesian Deep Learning. arXiv preprint arXiv:1712.00497. 2017.

132. Suk HI, Lee SW, Shen D. Alzheimer's disease neuroimaging initiative. Hierarchical feature representation and multimodal fusion with deep learning for AD/MCI diagnosis. Neuroimage. 2014;101:569–582. [PubMed: 25042445]

133. Brosch T, Tam R. Alzheimer's disease neuroimaging initiative. Manifold learning of brain MRIs by deep learning. Med Image Comput Assist Interv. 2013;16(pt 2):633–640.

134. Suk HI, Shen D. Deep learning-based feature representation for AD/MCI classification. Med Image Comput Assist Interv. 2013;16:583–590.

135. Li R, Zhang W, Suk HI, et al. Deep learning based imaging data completion for improved brain disease diagnosis. Med Image Comput Assist Interv. 2014;17:305–312.

136. Teramoto A, Fujita H, Yamamuro O, Tamaki T. Automated detection of pulmonary nodules in PET/CT images: ensemble false-positive reduction using a convolutional neural network technique. Med Phys. 2016;43:2821–2827. [PubMed: 27277030]

137. Li Z, Wang Y, Yu J, Guo Y, Cao W. Deep learning based radiomics (DLR) and its usage in noninvasive IDH1 prediction for low grade glioma. Sci Rep. 2017;7:5467. [PubMed: 28710497]

138. Teramoto A, Adachi H, Tsujimoto M, et al. Automated detection of lung tumors in PET/CT images using active contour filter. Proc SPIE. 2015;94142V.

139. Kimura H, Braun RD, Ong ET, et al. Fluctuations in red cell flux in tumor microvessels can lead to transient hypoxia and reoxygenation in tumor parenchyma. Cancer Res. 1996;56:5522–5528. [PubMed: 8968110]

140. Jain RK. Angiogenesis and lymphangiogenesis in tumors: insights from intravital microscopy. Cold Spring Harb Symp Quant Biol. 2002;67:239–248. [PubMed: 12858546]

141. Carmeliet P, Jain RK. Molecular mechanisms and clinical applications of angiogenesis. Nature. 2011;473:298–307. [PubMed: 21593862]

142. Dewhirst MW. Relationships between cycling hypoxia, HIF-1, angiogenesis and oxidative stress. Radiat Res. 2009;172:653–665. [PubMed: 19929412]

143. Gillies RJ, Gatenby RA. Metabolism and its sequelae in cancer evolution and therapy. Cancer J. 2015;21:88–96. [PubMed: 25815848]

144. O'Connor JP, Rose CJ, Waterton JC, Carano RA, Parker GJ, Jackson A. Imaging intratumor heterogeneity: role in therapy response, resistance, and clinical outcome. Clin Cancer Res. 2015;21:249–257. [PubMed: 25421725]

145. Chang YC, Ackerstaff E, Tschudi Y, et al. Delineation of tumor habitats based on dynamic contrast enhanced MRI. Sci Rep. 2017;7:9746. [PubMed: 28851989]

146. Han S, Stoyanova R, Lee H, et al. Automation of pattern recognition analysis of dynamic contrast-enhanced MRI data to characterize intratumoral vascular heterogeneity. Magn Reson Med. 2018;79:1736–1744. [PubMed: 28727185]

147. Gatenby RA, Silva AS, Gillies RJ, Frieden BR. Adaptive therapy. Cancer Res. 2009;69:4894–4903. [PubMed: 19487300]

148. Gatenby RA, Grove O, Gillies RJ. Quantitative imaging in cancer evolution and ecology. Radiology. 2013;269:8–15. [PubMed: 24062559]

149. Junttila MR, de Sauvage FJ. Influence of tumour micro-environment heterogeneity on therapeutic response. Nature. 2013;501:346–354. [PubMed: 24048067]

150. Robertson-Tessi M, Gillies RJ, Gatenby RA, Anderson AR. Impact of metabolic heterogeneity on tumor growth, invasion, and treatment outcomes. Cancer Res. 2015;75:1567–1579. [PubMed: 25878146]

151. Henning EC, Azuma C, Sotak CH, Helmer KG. Multispectral tissue characterization in a RIF-1 tumor model: monitoring the ADC and T2 responses to single-dose radiotherapy. Part II. Magn Reson Med. 2007;57:513–519. [PubMed: 17326182]

152. Brurberg KG, Gaustad JV, Mollatt CS, Rofstad EK. Temporal heterogeneity in blood supply in human tumor xenografts. Neoplasia. 2008;10:727–735. [PubMed: 18592011]

153. Wu J, Cui Y, Sun X, et al. Unsupervised clustering of quantitative image phenotypes reveals breast cancer subtypes with distinct prognoses and molecular pathways. Clin Cancer Res. 2017;23:3334–3342. [PubMed: 28073839]

154. Therasse P, Arbuck SG, Eisenhauer EA et al. New guidelines to evaluate the response to treatment in solid tumors. European Organization for Research and Treatment of Cancer, National Cancer Institute of the United States, National Cancer Institute of Canada. J Natl Cancer Inst. 2000;92:205–216. [PubMed: 10655437]

155. Eisenhauer EA, Therasse P, Bogaerts J, et al. New response evaluation criteria in solid tumours: revised RECIST guideline (version 1.1). Eur J Cancer. 2009;45:228–247. [PubMed: 19097774]

156. Glunde K, Jacobs MA, Pathak AP, Artemov D, Bhujwalla ZM. Molecular and functional imaging of breast cancer. NMR Biomed. 2009;22:92–103. [PubMed: 18792419]

157. Gillies RJ, Beyer T. PET and MRI: is the whole greater than the sum of its parts? Cancer Res. 2016;76:6163–6166. [PubMed: 27729326]

158. Brindle K New approaches for imaging tumour responses to treatment. Nat Rev Cancer. 2008;8:94–107. [PubMed: 18202697]

159. Marino MA, Helbich T, Baltzer P, Pinker-Domenig K. Multiparametric MRI of the breast: a review. J Magn Reson Imaging. 2018;47:301–315. [PubMed: 28639300]

160. Winfield JM, Payne GS, Weller A, deSouza NM. DCE-MRI, DW-MRI, and MRS in cancer: challenges and advantages of implementing qualitative and quantitative multi-parametric imaging in the clinic. Top Magn Reson Imaging. 2016;25:245–254. [PubMed: 27748710]

161. Bogin L, Margalit R, Ristau H, Mispelter J, Degani H. Parametric imaging of tumor perfusion with deuterium magnetic resonance imaging. Microvasc Res. 2002;64:104–115. [PubMed: 12074636]

162. Sala E, Kataoka MY, Priest AN, et al. Advanced ovarian cancer: multiparametric MR imaging demonstrates response- and metastasis-specific effects. Radiology. 2012;263:149–159. [PubMed: 22332064]

163. Riches SF, Payne GS, Morgan VA, et al. Multivariate modelling of prostate cancer combining magnetic resonance derived T2, diffusion, dynamic contrast-enhanced and spectroscopic parameters. Eur Radiol. 2015;25:1247–1256. [PubMed: 25749786]

164. Vannier MW, Butterfield RL, Jordan D, Murphy WA, Levitt RG, Gado M. Multispectral analysis of magnetic resonance images. Radiology. 1985;154:221–224. [PubMed: 3964938]

165. Vannier MW, Butterfield RL, Rickman DL, Jordan DM, Murphy WA, Biondetti PR. Multispectral magnetic resonance image analysis. Crit Rev Biomed Eng. 1987;15:117–144. [PubMed: 3691157]

166. Vannier MW, Pilgram TK, Speidel CM, Neumann LR, Rickman DL, Schertz LD. Validation of magnetic resonance imaging (MRI) multispectral tissue classification. Comput Med Imaging Graph. 1991;15:217–223. [PubMed: 1913572]

167. Fan X, Zhang H, Meng S, Zhang J, Zhang C. Role of diffusion-weighted magnetic resonance imaging in differentiating malignancies from benign ovarian tumors. Int J Clin Exp Med. 2015;8:19928–19937. [PubMed: 26884905]

168. Rabasco P, Caivano R, Simeon V, et al. Can diffusion-weighted imaging and related apparent diffusion coefficient be a prognostic value in women with breast cancer? Cancer Invest. 2017;35:92–99. [PubMed: 28107084]

169. Lin YC, Lin G, Hong JH, et al. Diffusion radiomics analysis of intratumoral heterogeneity in a murine prostate cancer model following radiotherapy: pixelwise correlation with histology. J Magn Reson Imaging. 2017;46:483–489. [PubMed: 28176411]

170. Brynolfsson P, Nilsson D, Henriksson R, et al. ADC texture-an imaging biomarker for high-grade glioma? Med Phys. 2014;41:101903. [PubMed: 25281955]

171. Cabarrus MC, Westphalen AC. Multiparametric magnetic resonance imaging of the prostate-a basic tutorial. Transl Androl Urol. 2017;6:376–386. [PubMed: 28725579]

172. Yun BL, Cho N, Li M, et al. Intratumoral heterogeneity of breast cancer xenograft models: texture analysis of diffusion-weighted MR imaging. Korean J Radiol. 2014;15:591–604. [PubMed: 25246820]

173. Fehr D, Veeraraghavan H, Wibmer A, et al. Automatic classification of prostate cancer Gleason scores from multiparametric magnetic resonance images. Proc Natl Acad Sci U S A. 2015;112:E6265–E6273. [PubMed: 26578786]

174. Price JM, Robinson SP, Koh DM. Imaging hypoxia in tumours with advanced MRI. Q J Nucl Med Mol Imaging. 2013;57:257–270. [PubMed: 24045622]

175. Gordon Y, Partovi S, Muller-Eschner M, et al. Dynamic contrast-enhanced magnetic resonance imaging: fundamentals and application to the evaluation of the peripheral perfusion. Cardiovasc Diagn Ther. 2014;4:147–164. [PubMed: 24834412]

176. Jackson A, O'Connor JP, Parker GJ, Jayson GC. Imaging tumor vascular heterogeneity and angiogenesis using dynamic contrast-enhanced magnetic resonance imaging. Clin Cancer Res. 2007;13:3449–3459. [PubMed: 17575207]

177. Newbold K, Castellano I, Charles-Edwards E, et al. An exploratory study into the role of dynamic contrast-enhanced magnetic resonance imaging or perfusion computed tomography for detection of intratumoral hypoxia in head-and-neck cancer. Int J Radiat Oncol Biol Phys. 2009;74:29–37. [PubMed: 19036529]

178. Egeland TA, Gulliksrud K, Gaustad JV, Mathiesen B, Rofstad EK. Dynamic contrast-enhanced-MRI of tumor hypoxia. Magn Reson Med. 2012;67:519–530. [PubMed: 21661044]

179. Stoyanova R, Huang K, Sandler K, et al. Mapping tumor hypoxia in vivo using pattern recognition of dynamic contrast-enhanced MRI data. Transl Oncol. 2012;5:437–447. [PubMed: 23326621]

180. Chaudhury B, Zhou M, Goldgof DB, et al. Heterogeneity in intratumoral regions with rapid gadolinium washout correlates with estrogen receptor status and nodal metastasis. J Magn Reson Imaging. 2015;42:1421–1430. [PubMed: 25884277]

181. Carano RA, Ross AL, Ross J, et al. Quantification of tumor tissue populations by multispectral analysis. Magn Reson Med. 2004;51:542–551. [PubMed: 15004796]

182. Henning EC, Azuma C, Sotak CH, Helmer KG. Multispectral quantification of tissue types in a RIF-1 tumor model with histological validation. Part I. Magn Reson Med. 2007;57:501–512. [PubMed: 17326181]

183. Barck KH, Willis B, Ross J, French DM, Filvaroff EH, Carano RA. Viable tumor tissue detection in murine metastatic breast cancer by whole-body MRI and multispectral analysis. Magn Reson Med. 2009;62:1423–1430. [PubMed: 19859948]

184. Berry LR, Barck KH, Go MA, et al. Quantification of viable tumor microvascular characteristics by multispectral analysis. Magn Reson Med. 2008;60:64–72. [PubMed: 18421695]

185. Fahridzadeh H, Chaudhury B, Scott JG, et al. Signal intensity analysis of ecological defined habitat in soft tissue sarcomas to predict metastasis development. Proc SPIE Med Imaging 2016: CADx. 2016;9785:97851H. doi.10.1117/12.2216961.

186. Fahridzadeh H, Chaudhury B, Zhou M, et al. Prediction of treatment outcome in soft tissue sarcoma based on radiologically defined habitats. Proc SPIE Med Imaging 2015: CADx. 2015;9414:94141U. doi.10.1117/12.2082324.

187. Stringfield O, Arrington J, Sahebjam S, Raghunand N. Multiparameter MRI response assessment in a phase I trial of hypofractionated stereotactic irradiation with pembrolizumab and bevacizumab in patients with recurrent high grade gliomas. Proc Intl Soc Mag Reson Med. 2016;24:3535.

188. Zhou M, Hall L, Goldgof D, et al. Radiologically defined ecological dynamics and clinical outcomes in glioblastoma multiforme: preliminary results. Transl Oncol. 2014;7:5–13. [PubMed: 24772202]

189. Zhou M, Chaudhury B, Hall LO, Goldgof DB, Gillies RJ, Gatenby RA. Identifying spatial imaging biomarkers of glioblastoma multiforme for survival group prediction. J Magn Reson Imaging. 2017;46:115–123. [PubMed: 27678245]

190. Lee J, Narang S, Martinez J, Rao G, Rao A. Spatial habitat features derived from multiparametric magnetic resonance imaging data are associated with molecular subtype and 12-month survival status in glioblastoma multiforme. PLoS One. 2015;10: e0136557. [PubMed: 26368923]

191. Lee J, Narang S, Martinez JJ, Rao G, Rao A. Associating spatial diversity features of radiologically defined tumor habitats with epidermal growth factor receptor driver status and 12-month survival in glioblastoma: methods and preliminary investigation. J Med Imaging (Bellingham). 2015;2:041006. [PubMed: 26835490]

192. Vriens D, Disselhorst JA, Oyen WJ, de Geus-Oei LF, Visser EP. Quantitative assessment of heterogeneity in tumor metabolism using FDG-PET. Int J Radiat Oncol Biol Phys. 2012;82:e725–e731. [PubMed: 22330998]

193. Metz S, Ganter C, Lorenzen S, et al. Phenotyping of tumor biology in patients by multimodality multiparametric imaging: relationship of microcirculation, v3 expression, and glucose metabolism. J Nucl Med. 2010;51:1691–1698. [PubMed: 20956471]

194. Schmitz J, Schwab J, Schwenck J, et al. Decoding intratumoral heterogeneity of breast cancer by multiparametric in vivo imaging: a translational study. Cancer Res. 2016;76:5512–5522. [PubMed: 27466286]
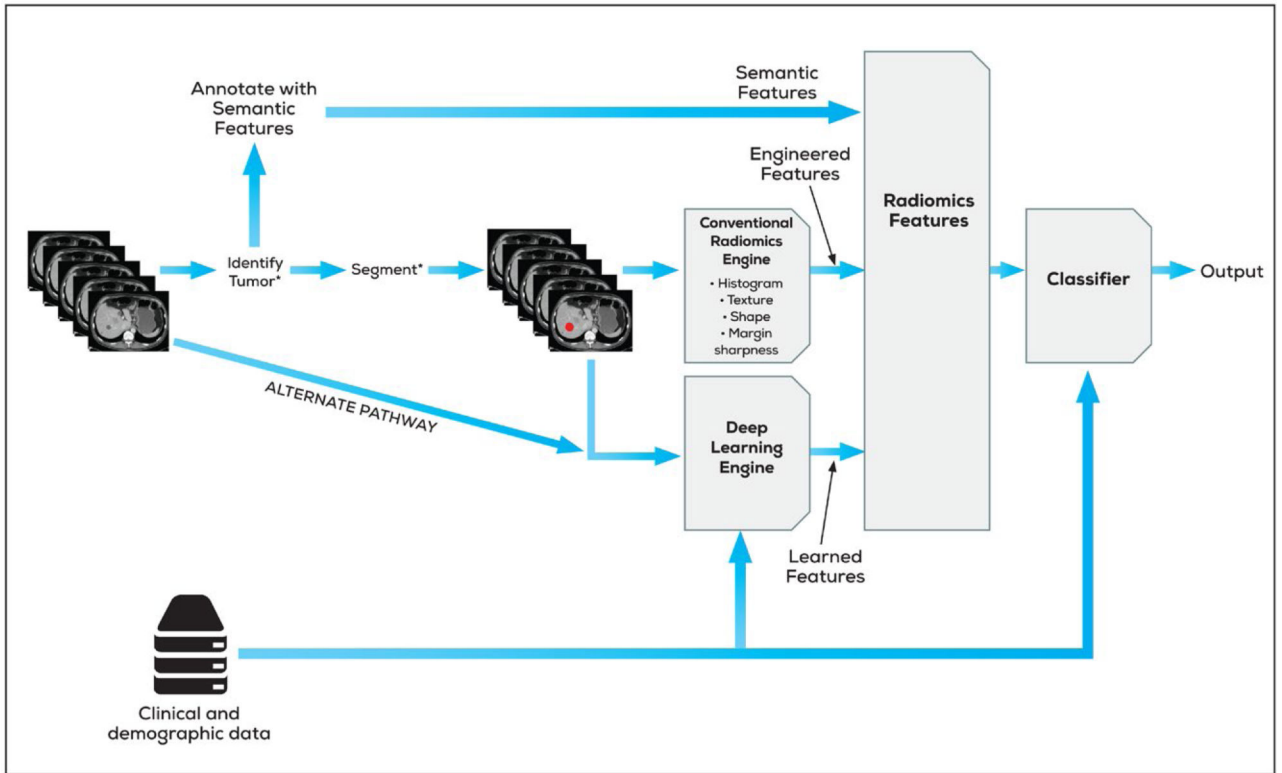
Figure 1.
Radiomics workflows. The conventional workflow computes human-engineered features, whereas the deep learning workflow explores features during training using labeling from clinical and/or demographic data. Either workflow can be used, or both can be used and the resulting features combined. The deep learning workflow can use, but may not require, tumor identification or segmentation (hence "alternate pathway"). Both workflows also can use semantic features for the final classification stage, which generates an output such as benign/malignant, responder/nonresponder, probability of 5-year survival, etc.

Figure 2.
Example of semantic annotation of a lung tumor that is part solid and part ground glass using ePAD. After tumor segmentation (green), either manually within ePAD or created via other means, an observer selects annotations using a custom template (eg, one that was built using the AIM Template Builder)[33] or one of several available templates. The example in this figure shows a subset of the annotation topics that are required to complete this annotation.
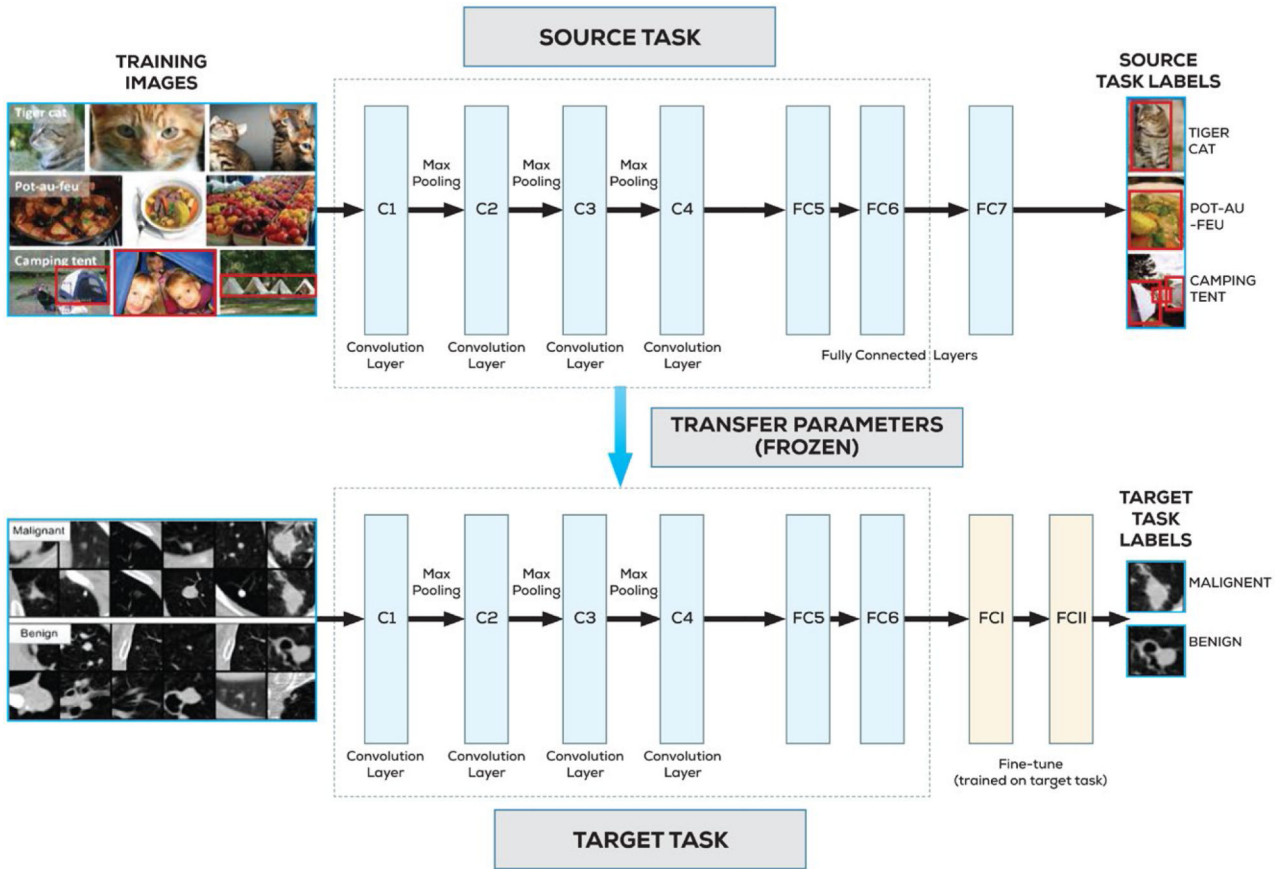
Figure 3.

Schematic representation of convolutional neural network (CNN) architecture and the concept of "transfer learning." Because images from multiple sources have common salient features (borders, shapes, etc), the core of a CNN trained for 1 task (*Top row*: eg, cat from pot-au-feu from camping tent) can be "transferred" (ie, used without modification) for a second task (*Bottom row*: benign from malignant tumors in computed tomography images). Because only the distal layers (fully connected [FC] I and FCII) remain to be trained, much less training data are required for the second task. Max indicates maximum.
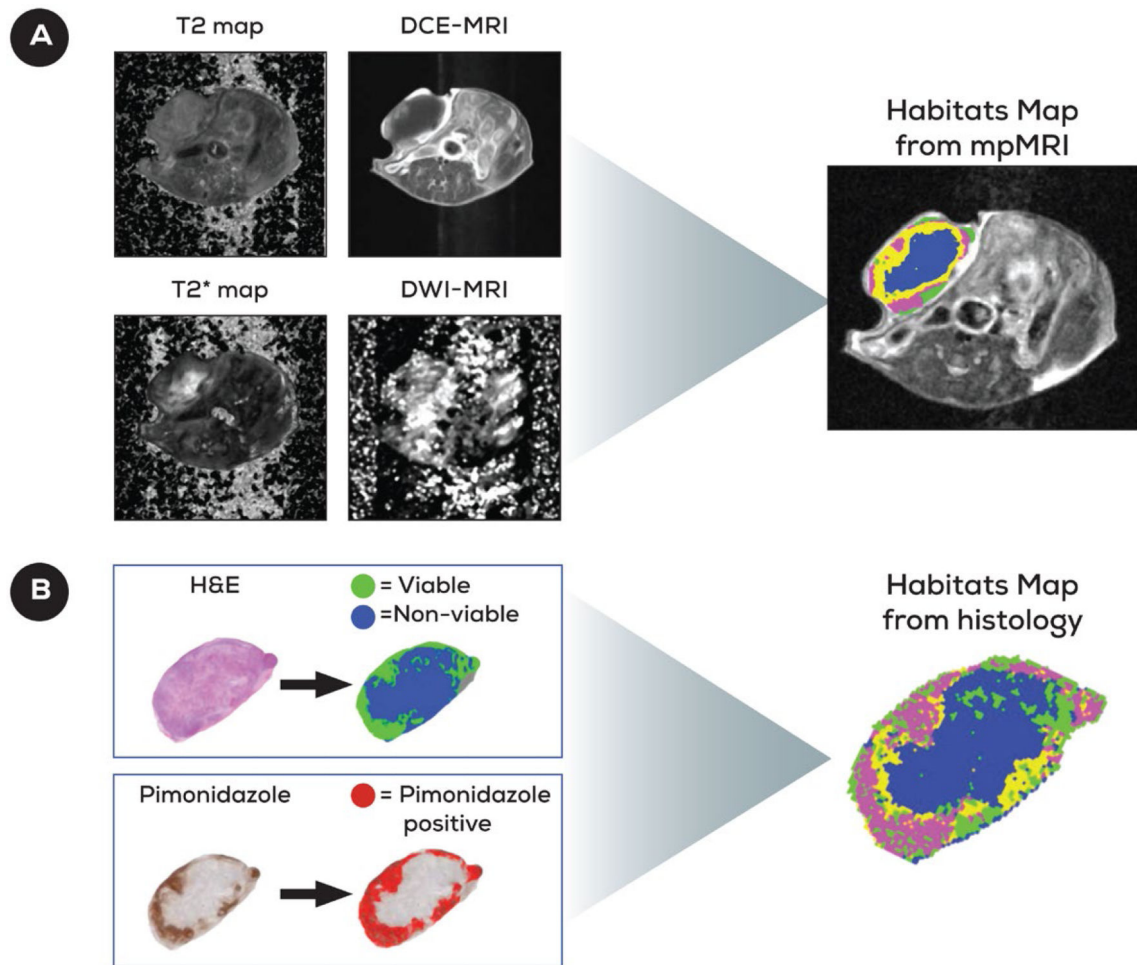
Figure 4.
Multiparametric magnetic resonance imaging (mpMRI) data used to identify tumor subregions ("habitats") in a 4T1 breast cancer allograft in a mouse model. (A) Parameters derived from T2 map, T2* map, diffusion-weighted (DWI)-MRI, and dynamic contrast-enhanced (DCE)-MRI were clustered to create a habitat map, demonstrating 4 intratumor subpopulations with different patterns of cellularity. Blue indicates necrotic; yellow, nonviable hypoxic; pink, viable hypoxic; green, viable nonhypoxic. (B) A coregistered habitat map derived from histology demonstrating good spatial correspondence with the habitat map derived from MRI. Histological slices were obtained by cutting the tumors using a 3-dimensional printed mold, which ensured the coregistration with MRI slices. Hematoxylin and eosin (H&E) and immunohistochemistry images were automatically segmented and superimposed to create habitat maps derived from histology, showing necrosis (blue), viable normoxic (green), pimonidazole in a viable region (pink), and pimonidazole in a nonviable region (yellow).
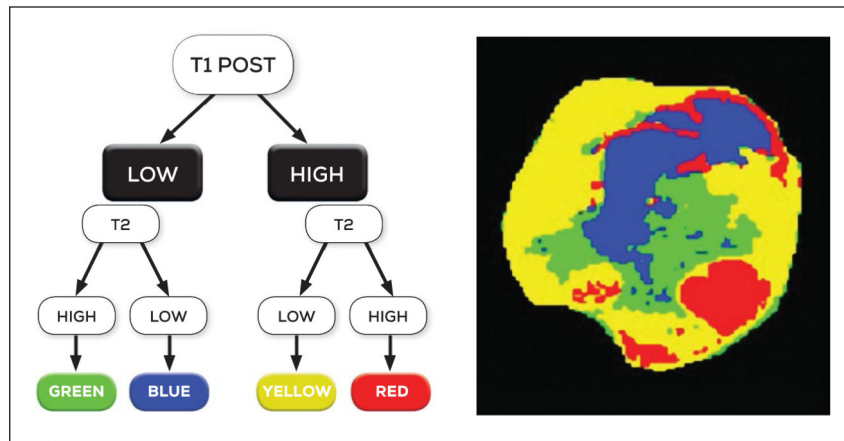
Figure 5.

Multiparametric magnetic resonance imaging (mpMRI) habitats in patients with soft tissue sarcoma. Otsu thresholding was used to separate postcontrast T1 images into low (L) and high (H) intensities. Within each of these subsets, Otsu thresholding again was used to separate quantitative T2 images into L and H, generating 4 habitats: L-H (indicated in green), L-L (indicated in blue), H-L (indicated in yellow), and H-H (indicated in red). The occurrence of the yellow habitat was the only significant predictor of outcome in univariate analyses (in cases in which this habitat occupied >18% of the tumor volume, progression-free survival and overall survival were significantly worse).
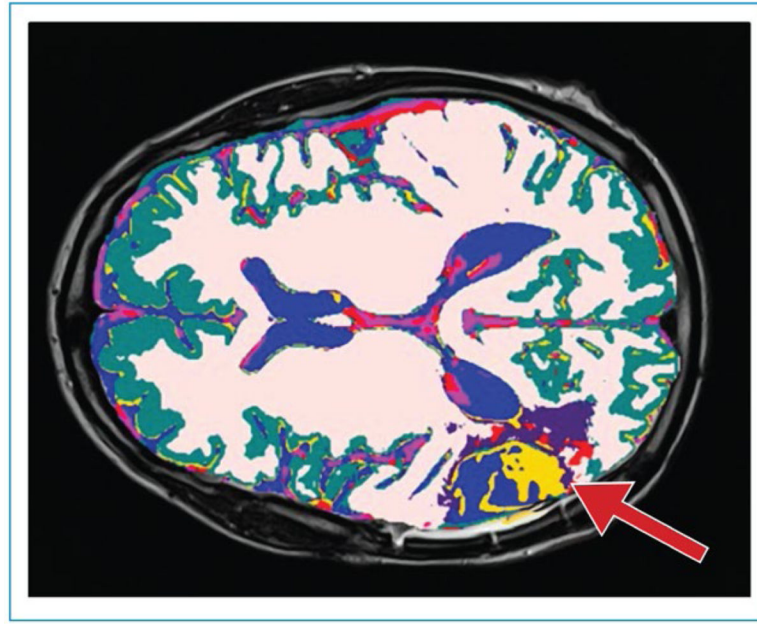
Figure 6.
Five coregistered magnetic resonance imaging (MRI) sequences, namely apparent diffusion coefficient, T1 precontrast, T1 postcontrast, T2 weighted, and fluidattenuated inversion recovery (FLAIR), were combined to generate this map containing 7 habitats. The entire brain was clustered to identify normal and abnormal tissue classes. Note that this provides an automatic delineation of the tumor (arrow) along with its accompanying subregions.